Eurographics / IEEE Symposium on Visualization 2011 (EuroVis 2011)
H. Hauser, H. Pfister, and J. J. van Wijk
(Guest Editors)

Volume 30 (2011), Number 3

Lagrangian Coherent Structures with Guaranteed Material Separation

T. Germer[1], M. Otto[1], R. Peikert[2] and H. Theisel[1]

[1]University of Magdeburg, Germany
[2]ETH Zurich, Switzerland

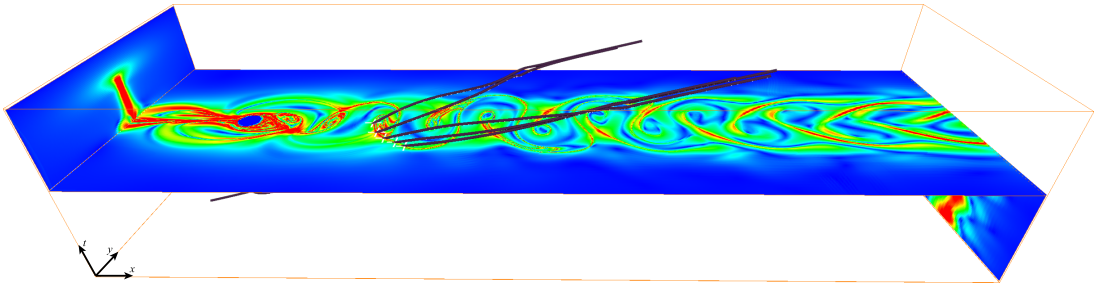

Figure 1: *Scalar field on a space-time parameterization of a cylinder flow. All separating structures in space-time are described by this field. The dark lines are 5 different path lines.*

Abstract

Given an unsteady flow field, one common way to compute Lagrangian Coherent Structures (LCS) is to extract extremal structures of the Finite Time Lyapunov Exponent (FTLE). Experience has shown that the resulting structures are often close to material structures (i.e., material lines or material surfaces). Moreover, it has been proven that for an integration time converging to infinity, they converge to exact material structures. However, due to the finite integration time in FTLE, they are generally not exact material structures.

In this paper we introduce a modification of the FTLE method which is guaranteed to produce separating material structures as features of a scalar field. We achieve this by incorporating the complete available integration time both in forward and backward direction, and by choosing an appropriate definition for separating structures. We apply our method to a number of test data sets and show the differences to classical FTLE.

1. Introduction

Nowadays, flow visualization has to deal with highly complex data sets. To manage this complexity, the extraction of topological features has gained major interest in the visualization community. However, approaches from vector field topology do not apply well to unsteady vector fields because the meaning of stream lines in time-dependent flows is limited. Here, the features are mainly related to the Lagrangian viewpoint. This has lead to the concept of Lagrangian Coherent Structures (LCS) which define regions of coherent flow behavior. As the name implies, these structures are advected in the flow. Thus, there is zero flux across these structures.

A common way to find LCS is to compute the Lyapunov Exponent (LE) and find its ridges [Lia66]. The LE characterizes the rate of separation of infinitesimally close trajectories. While the LE is computed for infinite time, we have to deal with data sets of finite time in practice. This has lead to the notion of Finite Time Lyapunov Exponents (FTLE), where the LE is computed over fixed time intervals [Hal01]. Also in this paper, we focus on finite-time data sets.

It has been shown, that the ridges of FTLE fields approximate LCS [Hal01]. However, FTLE ridges are not exact material structures and therefore deviate from LCS, as we analyze in section 4 using a number of counterexamples.

In this paper, we develop a modification of the FTLE method in order to find separating structures that are guaranteed material structures. Analogously to the FTLE method, we compute a scalar field that describes LCS, which we call Material Separation Field (MSF). Using this scalar field, we introduce an appropriate definition for separating structures,

which leads to material structures. We achieve the material separation by incorporating all available time steps to compute the scalar field. With our method, we have zero flux across separating structures and path lines always have constant MSF values. Therefore, separating structures found in one time step can easily be integrated to other time steps. The main contributions of this paper are:

- We analyze the fact that FTLE ridges are not exact material structures and show the relevance of this problem on different examples.
- We introduce a modification of the FTLE method which is guaranteed to produce separating structures that are material structures. Our MSF method is novel and produces material structures that separate regions of coherent flow behavior.
- We apply our method to three different test data sets and discuss the differences to FTLE methods.

2. Related Work

The extraction and visualization of Lagrangian Coherent Structures (LCS) has attracted scientists in CFD and visualization for almost a decade. One of the most prominent approaches for this is the computation of ridge structures in FTLE fields, as introduced by Haller [Hal01, HY00]. FTLE ridges have been used for a variety of applications [LCM*05, Hal02, SLP*09, WPJ*08]. Shadden et al. [SLM05] have shown that ridges of FTLE are approximate material structures, i.e., they converge to material structures for increasing integration times. This fact was used in [SW10] to extract topology-like structures and in [LM10] to accelerate the FTLE computation in 2D flows. Also in the visualization community, different approaches have been proposed to increase performance, accuracy and usefulness of FTLE as a visualization tool [SP09, GLT*09, GGTH07, SP07, SRP11, KPH*09]. Surveys on different flow visualization methods can be found in [PVH*03, LHZP07].

A crucial part of FTLE ridge extraction is the choice of a suitable ridge definition. Ridge definition and extraction is an active field of research in computer vision, computer graphics, and visualization. A variety of ridge definitions has been proposed in the literature. We mention local conditions obtained by relaxing conditions of extremal structures [EGM*94, Lin98], topological/watershed approaches [SWTH07], second derivative ridges [LM10] or definitions based in extremal curvature structures [OBS04]. [PS08, STS10] focus on the extraction of ridge surfaces in 3D fields. None of the ridge definitions mentioned above is sufficient to guarantee material separation for MSF. Because of this we will introduce another definition of separating structures based on the level sets of the MSF (see section 5.4). This can be regarded as a special case of the pathline predicates approach [SGSM08] which applies a boolean function to each pathline and separates the data set into two set of pathlines.

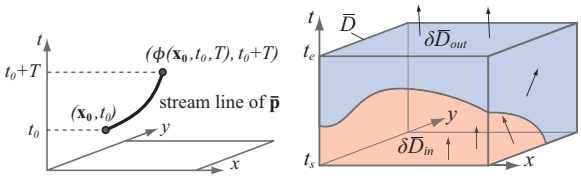

Figure 2: *(a) The stream line integration of* $\bar{\mathbf{p}}$ *starting from* $(\mathbf{x}_0,t_0)$ *over the integration time* T *ends at* $(\phi(\mathbf{x}_0,t_0,T),t_0+T)$. *(b) Example of domains of a 2D flow:* D *is rectangular,* $\bar{D}$ *is a (volumetric) box,* $\delta\bar{D}$ *is the surface of the box,* $\delta\bar{D}_{in}$ *denotes regions of inflow,* $\delta\bar{D}_{out}$ *denotes regions of outflow.*

3. Notation

In this section, we want to characterize our input data and clear the notation used throughout this paper.

Given is an n-dimensional ($n=2,3$) time dependent vector field $\mathbf{v}(\mathbf{x},t)$ over the space-time domain $\bar{D}=D\times[t_s,t_e]$ where $D\subset\mathbb{R}^n$ is a compact and closed set acting as the spatial domain of $\mathbf{v}$ and $[t_s,t_e]$ is the time interval on which $\mathbf{v}$ is given. Furthermore, let δD be the boundary of D. Then the boundary of the space-time domain is

$$\delta\bar{D}=D\times\{t_s,t_e\}\ \cup\ \delta D\times[t_s,t_e]. \tag{1}$$

We use the notation $\lambda_i(\mathbf{M})$ and $\mathbf{e}_i(\mathbf{M})$ for the i-th eigenvalue and corresponding eigenvector of a matrix $\mathbf{M}$, and $\lambda_{max}(\mathbf{M})$ for its maximal eigenvalue. Furthermore, let $\mathbf{M}^*$ be the transposed of $\mathbf{M}$.

The *flow map* $\phi_t^T(\mathbf{x})=\phi(\mathbf{x},t,T)$ of $\mathbf{v}$ is defined as the location of a particle seeded at $(\mathbf{x},t)$ after a path line integration of $\mathbf{v}$ over a time interval T. Given the spatial gradient

$$\Delta=\Delta(\mathbf{x},t,T)=\frac{d\phi(\mathbf{x},t,T)}{d\mathbf{x}} \tag{2}$$

of ϕ, the FTLE is computed as follows:

$$\mathrm{FTLE}(\mathbf{x},t,T)=\frac{1}{T}\ln\sqrt{\lambda_{max}(\Delta^*\cdot\Delta)} \tag{3}$$

In order to simplify some concepts, we can interpret the n-dimensional unsteady vector field $\mathbf{v}$ as a steady $(n+1)$-dimensional vector field

$$\bar{\mathbf{p}}(\mathbf{x},t)=\begin{pmatrix}\mathbf{v}(\mathbf{x},t)\\1\end{pmatrix}. \tag{4}$$

(The bar denotes that $\bar{\mathbf{p}}$ is a $(n+1)$-dimensional vector field in $\bar{D}$.) It is known that path lines of $\mathbf{v}$ correspond to stream lines of $\bar{\mathbf{p}}$ [TWHS05]. For $\bar{\mathbf{p}}$ we define the $(n+1)$-dimensional flow map

$$\bar{\phi}(\mathbf{x},t,T)=(\phi(\mathbf{x},t,T)\ ,\ t+T) \tag{5}$$

Figure 2a gives an illustration for $n=2$.

The field $\bar{\mathbf{p}}$ segments the boundary of the space-time domain $\delta\bar{D}$ into areas of inflow and outflow:

$$\delta\bar{D}_{in} = \{(\mathbf{x},t) \in \delta\bar{D} : \exists\, \varepsilon_0 > 0 \;\; \forall \varepsilon \in (0,\varepsilon_0) : (\mathbf{x},t) + \varepsilon\bar{\mathbf{p}}(\mathbf{x},t) \in \bar{D}\}$$
$$\delta\bar{D}_{out} = \{(\mathbf{x},t) \in \delta\bar{D} : \exists\, \varepsilon_0 > 0 \;\; \forall \varepsilon \in (0,\varepsilon_0) : (\mathbf{x},t) + \varepsilon\bar{\mathbf{p}}(\mathbf{x},t) \notin \bar{D}\}$$

Obviously, $D \times \{t_s\} \subseteq \delta\bar{D}_{in}$ and $D \times \{t_e\} \subseteq \delta\bar{D}_{out}$. Figure 2b gives an illustration.

4. FTLE Ridges are not Material Lines

Experience has shown that ridges of FTLE coincide in many cases well with material structures. However, in general they are not exact material structures, no matter which ridge definition of a scalar field we use. Unless very long integration times are used, FTLE ridges can deviate considerably from material structures. To show this, we now present three examples where the FTLE ridges significantly differ from material structures. We start with two synthetic data sets, before we analyze the flow in a real data set.

4.1. Vanishing Ridges

Let $(\mathbf{x}_0,t_0) \in \bar{D}$ be a point on a ridge of FTLE$(\mathbf{x},t,T)$. There is only a certain part of $\bar{D}$ which has influence on FTLE$(\mathbf{x}_0,t_0,T)$: only the domain $D \times [t_0 - T, t_0 + T]$ is involved. If the ridge is a material structure, then the complete path line $\phi(\mathbf{x}_0,t_0,T)$ for any T must be on the ridge. We construct a simple counterexample where this is not the case. We define a flow field $\mathbf{w}$ as

$$\mathbf{w}(\mathbf{x},t) = \begin{cases} \mathbf{v}(\mathbf{x},t) & \text{for} \quad t_0 - T \le t < t_0 + T \\ \frac{t_0+T+\varepsilon-t}{\varepsilon}\,\mathbf{v}(\mathbf{x},t_0+T) & \text{for} \quad t_0 + T \le t < t_0 + T + \varepsilon \\ \mathbf{0} & \text{for} \quad t_0 + T + \varepsilon \le t < t_0 + 3T + \varepsilon \end{cases}$$

Note that $\mathbf{w}$ is obtained by a linear blending of an arbitrary vector field $\mathbf{v}$ and the zero vector field $\mathbf{0}$ in the time interval $[t_0 + T, t_0 + T + \varepsilon]$ for a certain positive blending time ε. Then $(\mathbf{x}_0,t_0)$ is an extremal point of the FTLE of $\mathbf{w}$ as well since $\mathbf{v}$ and $\mathbf{w}$ coincide in a sufficiently large neighborhood of $(\mathbf{x}_0,t_0)$. Let $\bar{\phi}_{\mathbf{w}}$ be the flow map of $\mathbf{w}$ and let $(\mathbf{x}_1,t_1) = \bar{\phi}_{\mathbf{w}}(\mathbf{x}_0,t_0,2T+\varepsilon)$ be a point on the path line of $\mathbf{w}$ starting from $(\mathbf{x}_0,t_0)$. Since $\mathbf{w}(\mathbf{x},t) = \mathbf{0}$ in a sufficiently large neighborhood of $(\mathbf{x}_1,t_1)$, no measure will detect it as part of a ridge. Hence, the ridge from $\mathbf{w}$ cannot include the path line starting from $(\mathbf{x}_0,t_0)$. Figure 3 gives an illustration. Over time, the FTLE values on the path line decrease, until they reach zero at $t = 2T + \varepsilon$. Therefore, the FTLE ridge terminates before the path line leaves $\bar{D}$. In contrast, our method produces separating structures that include the full path lines.

4.2. Cylinder Flow

For the cylinder flow dataset (described in section 6.2), we computed the cross flux at some of its FTLE ridges. We selected a few local maxima of FTLE and extracted the associated height ridges using the parallel vectors method [PS08].

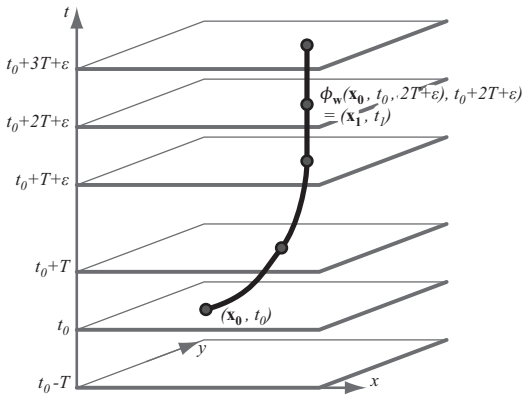

Figure 3: *Construction of a field* $\mathbf{w}$ *such that* $(\mathbf{x}_0,t_0)$ *is on a ridge but* $(\mathbf{x}_1,t_1)$ *is not. Hence the ridge is not a material structure.*

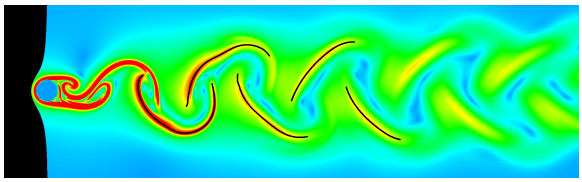

Figure 4: *FTLE field of the cylinder data set. The black lines indicate the ridges that we analyzed for cross flux.*

The FTLE field and the selected ridges are shown in figure 4. We use the common heat map technique discussed in section 5.3 for the visualization of the fields. For the FTLE computation we used backward integration of $T = 80$, where the data set has a total time span of 480. As we found the ridges to be distinct and clearly visible, we assume that T is long enough.

At a set of sample points per height ridge the flux per unit length was then computed by taking the velocity component orthogonal to the height ridge and subtracting the speed of the moving ridge in this orthogonal direction. The motion of the ridge was estimated by extracting height ridges from FTLE fields computed at a few earlier and later points in time (and verifying independence of the temporal sampling rate). Following Shadden et al. [SLM05], we divided this flux rate by the local velocity magnitude. This results in the percentages plotted in figure 5, which show relatively high values for the cross flux, ranging from -40 to over 10 percent. In figure 6 we extracted particles on one ridge and integrated them in the vector field for $T = 32$ and $T = -32$. The figure shows that the particles clearly deviate from the ridge and therefore cross it.

By applying this flux computation also to the "double gyre" field (see section 6.1), we were able to confirm Shadden's value of about 0.05% for the (rather long) integration

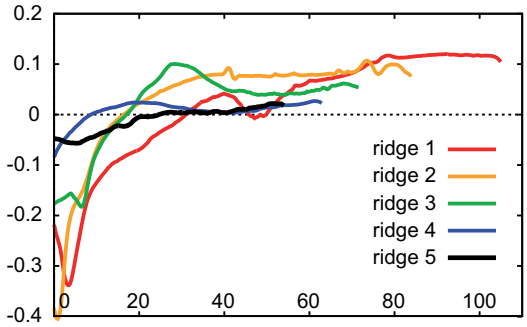

Figure 5: *Percentage of the flux crossing the five ridges from figure 4, plotted against ridge arc length.*

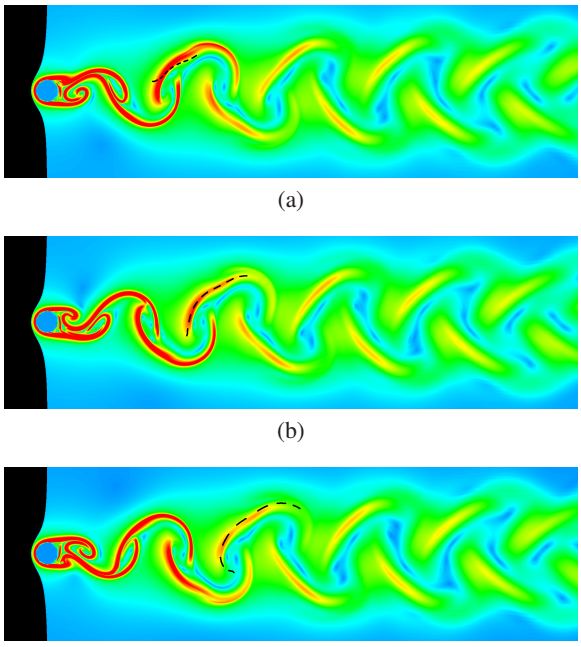

(a) (b) (c)

Figure 6: *Flux across FTLE ridges: the black line consists of particles integrated in the vector field, at (a) $T=-32$, (b) $T=0$ and (c) $T=32$.*

time $T=30$, while for $T=3$ we obtained similar cross flux percentages as for the cylinder flow example.

5. Material Separation Fields

We now describe our method, which produces separating material structures. The key idea is to define a modification of FTLE fields called "Material Separation Fields" (MSF) such that every point on a path line has the same MSF value, i.e.,

$$\mathrm{MSF}(\mathbf{x},t)=\mathrm{MSF}(\phi(\mathbf{x},t,T),t+T) \tag{6}$$

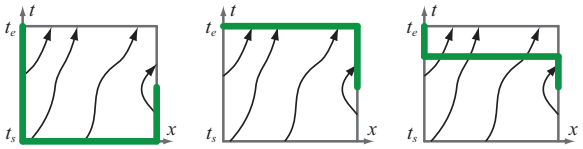

(a) (b) (c)

Figure 7: *Three parameterizations of the path lines of a 1D time-dependent vector field: (a) $\bar{P}_{t_s}$; (b) $\bar{P}_{t_e}$; (c) $\bar{P}_t$ with $t_s < t < t_e$. The green lines are the parameterizations: integrating from them covers the whole domain.*

for any integration time T which does not leave $\bar{D}$. Once we have this, an arbitrary point on a path line can serve as representative for computing MSF, and the MSF for all other points on the path line can simply be obtained by advection along $\bar{\mathbf{p}}$.

5.1. Parameterization of Path Lines

Since we need only one point per path line as representative, we search for subsets $\bar{P}$ of $\bar{D}$ with the property that every stream line of $\bar{\mathbf{p}}$ intersects $\bar{P}$ in exactly one point. Then the MSF only has to be computed on $\bar{P}$ and from there simply be advected to every location of $\bar{D}$. We call the definition of $\bar{P}$ the *parameterization of path lines*.

Parameterization is a well-studied concept for curves and surfaces, meaning to find an injective map from a subset of $\mathbb{R}^2/\mathbb{R}^3$ to a curve/surface. This map allows a unique addressing of every curve/surface point. Fortunately, for path lines there is a simple solution for the parameterization. Since the last component of $\bar{\mathbf{p}}$ is 1, it is guaranteed that the integration of $\bar{\mathbf{p}}$ starting from any point $(\mathbf{x},t)\in\bar{D}$ will leave $\bar{D}$ in a unique point on $\delta\bar{D}$ for both forward and backward direction. This gives two simple solutions: both $\delta\bar{D}_{in}$ and $\delta\bar{D}_{out}$ can act as the domain of the path line parameterization. Based on this we can even define a parameterization which is based on an arbitrary time slice $t=const$ as

$$\bar{P}_t=\{D\times\{t\}\}\cup\{(\mathbf{x},s)\in\delta\bar{D}_{in}|s>t\}\cup\{(\mathbf{x},s)\in\delta\bar{D}_{out}|s<t\}. \tag{7}$$

(7) has the special cases $\bar{P}_{t_s}=\delta\bar{D}_{in}$ and $\bar{P}_{t_e}=\delta\bar{D}_{out}$. Figure 7 illustrates the path line parameterization of a 1D vector field $u(x,t)$ for which we consider the 2D path line field $\bar{\mathbf{p}}(x,t)=(u(x,t),1)^T$. Figure 1 shows a parameterization in a practical example.

5.2. Defining MSF

Given a point $(\mathbf{x},t)\in\bar{D}$, we integrate $\bar{\mathbf{p}}$ until we leave $\bar{D}$ in a point $(\mathbf{x}_{out},t_{out})$ under forward and $(\mathbf{x}_{in},t_{in})$ under backward integration (in the implementation we also stop if one of the particles needed for the gradient computation leaves $\bar{D}$):

$$\begin{aligned}(\mathbf{x}_{in},t_{in}) &= \bar{\phi}(\mathbf{x},t,t_{in}-t)\\ (\mathbf{x}_{out},t_{out}) &= \bar{\phi}(\mathbf{x},t,t_{out}-t)\end{aligned} \tag{8}$$

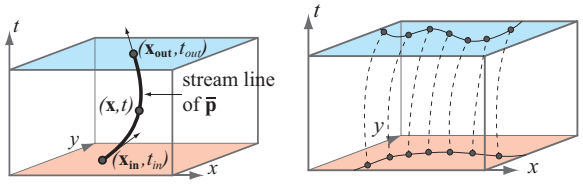

Figure 8: *(a) Integrating $\bar{\mathbf{p}}$ from $(\mathbf{x},t)$ leaves $\bar{D}$ in $(\mathbf{x}_{in},t_{in})$ and $(\mathbf{x}_{out},t_{out})$. (b) Separating structures of MSF on $\delta\bar{D}_{in}$ and $\delta\bar{D}_{out}$ are connected by path lines.*

with $(\mathbf{x}_{in},t_{in}) \in \delta\bar{D}_{in}$ and $(\mathbf{x}_{out},t_{out}) \in \delta\bar{D}_{out}$. Note that $t_s \leq t_{in} \leq t_{out} \leq t_e$. Figure 8a gives an illustration.

In order to compute $\mathrm{MSF}(\mathbf{x},t)$, we consider the whole path line from $(\mathbf{x}_{in},t_{in})$ to $(\mathbf{x}_{out},t_{out})$. We define

$$\begin{aligned} \Delta_M(\mathbf{x},t) &= \Delta(\mathbf{x}_{in},t_{in},t_{out}-t_{in}) \\ &= (\Delta(\mathbf{x},t,t_{in}-t))^{-1} \cdot \Delta(\mathbf{x},t,t_{out}-t). \end{aligned} \tag{9}$$

Therefore, $\Delta_M(\mathbf{x},t)$ expresses the gradient of the flow map from t_{in} to t_{out} at point $(\mathbf{x}_{in},t_{in})$. Note that $\Delta_M(\mathbf{x},t) = \Delta_M(\phi(\mathbf{x},t,T),t+T)$ for any T with $t_{in} \leq t+T \leq t_{out}$, meaning Δ_M stays constant along a given path line.

Now we can compute the forward MSF as

$$\mu_i = \frac{1}{t_{out}-t_{in}} \ln \sqrt{\lambda_i((\Delta_M)^* \cdot \Delta_M)} \tag{10}$$

and

$$\mathrm{MSF}_f = \max_{i=1..n} \mu_i. \tag{11}$$

In a similar way we can define the backward MSF:

$$\nu_i = \frac{1}{t_{out}-t_{in}} \ln \sqrt{\lambda_i((\Delta_M{}^{-1})^* \cdot \Delta_M{}^{-1})} \tag{12}$$

and

$$\mathrm{MSF}_b = \min_{i=1..n} \nu_i. \tag{13}$$

There is a simple relation between μ_i and ν_i:

$$\{\mu_i,...,\mu_n\} = \{-\nu_1,...,-\nu_n\}. \tag{14}$$

Therefore, $\mathrm{MSF}_f = -\mathrm{MSF}_b$. Because of this equivalence, we only use the forward MSF in the rest of this paper.

As can be seen from equations 10 and 11, the MSF is computed in a similar way to the FTLE (compare to equation 3). The FTLE uses a fixed integration time T. In contrast, we incorporate all available time steps from t_{in} to t_{out}. This means, that the forward and backward integration times can differ for different points. However, their sum always equals $t_{out}-t_{in}$. Because Δ_M is constant along a given path line, the MSF is also constant along that path line.

Given the parameterization of path lines as described in section 5.1, we now have a simple and efficient way to compute the MSF for all points $(\mathbf{x},t) \in \bar{D}$. We only need to compute the MSF on any parameterization $\bar{P}_t$. The MSF values for other points $(\mathbf{x},t)$ can then be found by looking up the intersection of the corresponding path line with $\bar{P}_t$. Therefore, the MSF of $\bar{D}$ can be regarded as a time-morph of the MSF of $\bar{P}_t$ along the vector field.

5.3. Time Period of Interest

Another consequence of constant MSF values along path lines is that our results represent mixtures of structures from forward and backward integration (called unstable and stable manifolds in [SLM05]). Both types of structures can cross and overlap each other. Such crossings are well illustrated in figure 9a and 11. The corresponding data sets are described in section 6. While this effect results from the material separation property, we still need a way to distinguish unstable and stable manifolds for practical use. We also would like to incorporate a way to analyze short term behavior that is decoupled from the temporal extent of the data set.

In order to address these issues, we provide an optional visualization technique. Commonly, heat maps are used for the visualization of FTLE fields. In this paper, we normalized the field values and mapped them to the color range shown figure 10a. For an alternative visualization, we introduce a time period of interest (POI) which represents a certain timeframe the user is interested in. The user provides three time stamps:

- t_c: defines the current time frame, where the MSF should be computed,
- t_s^{poi}: defines the start of the POI,
- t_e^{poi}: defines the end of the POI,

where $t_s^{poi} \leq t_c \leq t_e^{poi}$. In addition to the gradient of the flow map for the whole domain (Δ_M, see section 5.2), we similarly compute the gradient Δ_{poi} for the domain $D \times [t_s^{poi},t_e^{poi}]$, which is restricted by the POI. Using this gradient, we compute the MSF for the POI:

$$\mathrm{MSF}_{poi} = \max_{i=1..n} \frac{1}{t_{out}-t_{in}} \ln \sqrt{\lambda_i((\Delta_{poi})^* \cdot \Delta_{poi})}. \tag{15}$$

Finally, we compute the value $\sigma = MSF/MSF_{poi}$, which describes the portion of separation that exists within the POI. Note that we need the term $t_{out}-t_{in}$ (instead of $t_e^{poi}-t_s^{poi}$) in equation 15 in order to put these two quantities in relation.

For the alternative visualization, we map MSF values to pixel intensity and σ to the saturation of red (see figure 10b). Therefore, structures with strong separating behavior within the POI appear red, while structures with separation outside the POI appear gray and desaturated. This way, we can highlight stable manifolds using $t_s^{poi} = t_{in}$ and $t_e^{poi} = t_c$, as can be seen in figure 9b. Analogously, unstable manifolds are highlighted by setting $t_s^{poi} = t_c$ and $t_e^{poi} = t_{out}$ (see figure 9c). Short term structures can also be emphasized by using different values for t_s^{poi} and t_e^{poi}, that are near t_c (see figure 9d).

In the context of MSF, the drawback of this visualization

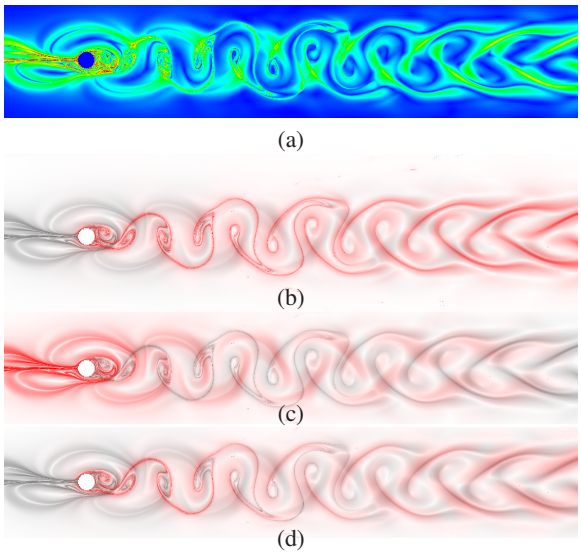

Figure 9: *Time periods of interest for the MSF at $t = 240$: (a) heat map for $t = 240$, (b) $t_{poi} = [0, 240]$, (c) $t_{poi} = [240, 480]$, (d) $t_{poi} = [120, 240]$*

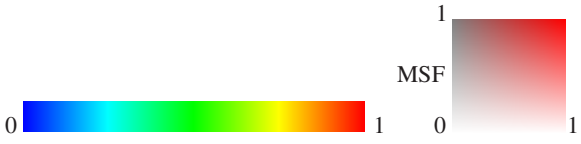

Figure 10: *Color scheme*

technique is that color values do not represent material structures anymore. Nevertheless, we regard this technique as a compromise, because material structures can still be recognized from the intensity values.

The field values are normalized and mapped to the color range shown figure 10.

5.4. Appropriate Separating Structures

The fact that the MSF is constant along path lines does not guarantee material separation yet. In addition, we have to use an appropriate extraction of separating structures. However, all ridge definitions we are aware of fail to extract material structures as ridges. We propose a simple definition of MSF separating structures which guarantees material separation.

Instead of a central ridge line, we regard level sets of the MSF as separating structures, that is

$$s_c(t) = \{\mathbf{x} : MSF(\mathbf{x}, t) = k\}, \tag{16}$$

where k is a user defined constant. Per default, we choose k such that

$$f(k) = \frac{number\ of\ saddle\ points\ inside\ s_c(t)}{\sqrt{area\ enclosed\ by\ s_c(t)}} \tag{17}$$

is maximal. This formulation is motivated by the observation that in the discrete setting ridges are composed of a sequence of alternating saddles and maxima. Therefore, these level sets surround MSF maxima tightly and enclose regions with ridge-like behavior. Because high MSF values mark separating flow behavior, the level sets represent volumetric regions (instead of lines) that separate different flow behavior. Note that a similar view point has been taken in the field of vortex extraction, where both line structures (vortex core lines) and volumetric regions are well excepted approaches for vortex characterization. In a similar way, we propose a region approach for the separating structures. In the context of steady-state flow, the approach of representing separation behavior with regions was also described in [CMLZ08].

Because MSF values are constant along path lines and level sets define the subspaces of points with constant MSF values, the level sets stay on path lines. Therefore, our separating structures are material structures.

Alternatively, we could consider the regions inside the level sets $s_r(t) = \{\mathbf{x} : MSF(\mathbf{x}, t) > k\}$ as separating structures. Again, these regions stay on path lines and are deformed by the vector field. Computing them can be done by a simple thresholding of the MSF.

Given a suitable threshold k, our separating structures tightly enclose the ridges of the MSF. Therefore, they describe ridge-like regions, in which the flow is mostly parallel to the enclosed ridge. Still, our separating structures are elongated like ridges and separate the flow on both sides of the structure. Our formulation of separating structures as volumetric regions represents an alternative to the notion of ridges that represents flow separation, but also leads to material structures as well as the segmentation of ridge-like flow behavior.

Our definition of separating structures means that they are connected by path lines. In particular, this holds for separating structures on $\delta\bar{D}_{in}$ and $\delta\bar{D}_{out}$ (see figure 8b). Thus, if we are interested in the separating structures of $\bar{D}$, we only need to compute the separating structures on any parameterization $\bar{P}_t$ (like $\delta\bar{D}_{in}$ or $\delta\bar{D}_{out}$) and advect them in the vector field like material structures. The parameterization and constant MSF of the path lines guarantees that all separating structures are found.

6. Examples

We implemented and tested the MSF method on a 3.2 GHz four core PC. All data sets were sampled on a regular 3D grid representing space-time. We used a fourth-order Runge-Kutta scheme and trilinear interpolation for the integration of path lines. The integration was carried out on the GPU (GeForce GTX 260) using CUDA. We computed the gradient of the flow map using finite differencing of neighboring particles as described in [SLM05]. The computation time

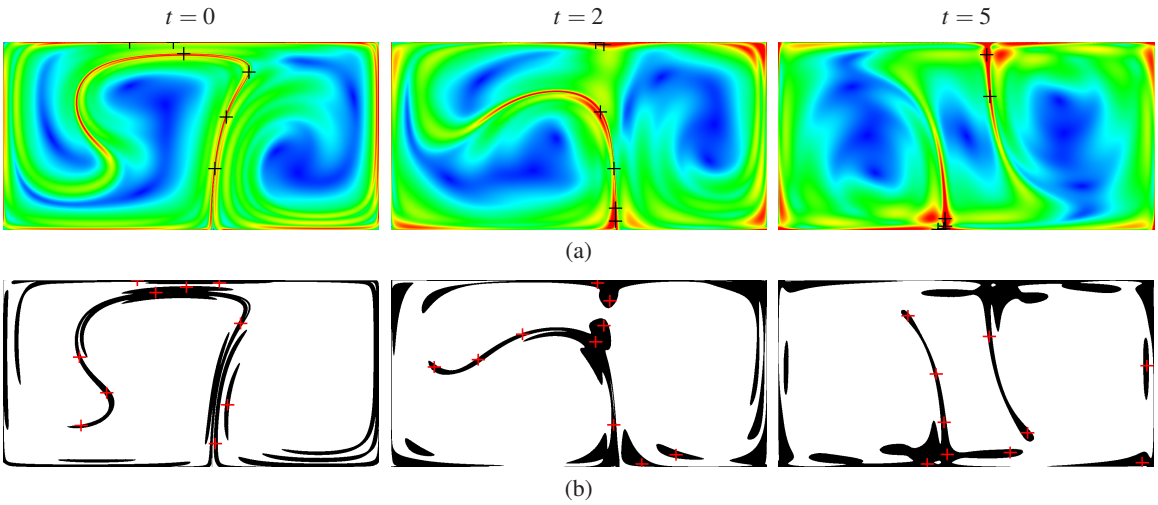

Figure 11: *Double Gyre example: (a) MSF, (b) MSF separating structures. The black and red crosses show particles advected by the flow.*

mainly depends on the number of output pixels and the integration steps for each path line. Therefore, it also depends on the total time span of the data set. Corresponding to other FTLE visualization papers, we mapped the scalar field values to color hue, where blue means low value and red means high value. In the following, we present our results using three examples.

6.1. Double Gyre

Our next example is the double gyre data set, which was introduced in [SLM05]. It is computed using the following functions:

$$f(x,y,t) = a(t)x^2 + b(t)x \tag{18}$$
$$a(t) = \varepsilon\, sin(\omega t)$$
$$b(t) = 1 - 2\varepsilon\, sin(\omega t)$$

The vector field at point (x,y) at time t is given by:

$$u = -\pi A\, sin(\pi f(x))\, cos(\pi y) \tag{19}$$
$$v = \pi A\, cos(\pi f(x))\, sin(\pi y) \frac{df}{dx}$$

The domain for this data set is $D = [0,2] \times [0,1]$. We used the parameters $A = 0.1, \omega = \frac{2\pi}{10}$ and $\varepsilon = 0.25$.

First, we consider the time span $t = [0,10]$, consisting of one full period of the double gyre motion. We sampled space-time with a $200 \times 100 \times 100$ grid. Figure 11a shows the resulting MSF at different points in time. Figure 11b shows the corresponding separating structures. The threshold k of the level set is determined by the maximum of $f(k)$ displayed in figure 13a. We refer to the accompanying video for an animation of the full sequence. The computation time for one picture was approximately 15 seconds. The black and red crosses mark particles that are seeded by hand and advected in the flow. Note that they do not cross the separating structures at any time. This confirms our statement that MSF separating structures are indeed material structures.

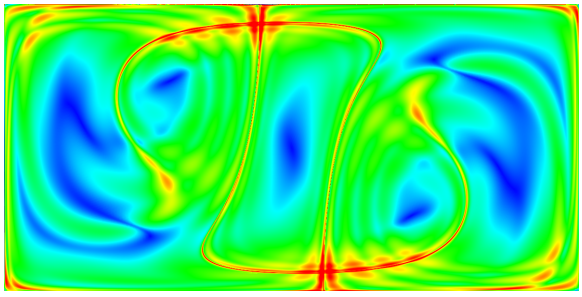

Figure 12: *Double period of the double gyre (t=[0,20]) at t=10. The more periods are considered, the more the separating structures cross.*

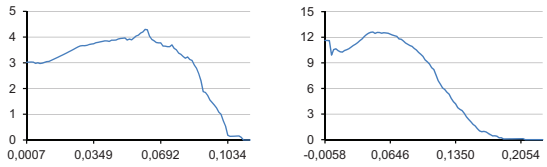

(a) (b)

Figure 13: *Plot of $f(k)$ (equation 17) against k: (a) double gyre with a maximum of $f(k)$ at a MSF value of $k = 0.06$, (b) cylinder with a maximum of $f(k)$ at $k = 0.046$.*

Both separating structures from forward and backward integration are visible. At $t = 0$ only structures from forward integration are extracted. As t grows, separating structures from backward integration develop and cross the forward

structures. Particles at these crossings flow into both saddle regions on the top edge under forward integration and on the bottom edge under backward integration. If we enlarge the time span of the data sets, the separating structures become more complex and cross each other more often. Figure 12 shows an MSF of the double gyre data set with two periods.

6.2. Cylinder Flow

In the third example, we analyzed a data set of a flow around a circular cylinder that was simulated on an irregular grid. This grid was uniformly resampled onto a regular grid with dimension $560 \times 160 \times 61$. The time span of the data set is $t = [0, 480]$.

Figure 15a shows the MSF of four time steps. The accompanying video includes an animation of the full sequence. The computation time was approximately 40 seconds per picture. The corresponding structures in figure 15b clearly separate regions of different flow behavior. The threshold k of the level set is determined by the maximum of $f(k)$ displayed in figure 13b. Again, the black and red crosses mark the position of five particles that are advected in the flow. In contrast to the FTLE ridges in figure 4, the particles do not cross the separating structures and stay on them.

In figure 14, we show different path line parameterizations. The MSF on the inflow boundary $\delta\bar{D}_{in}$ and outflow boundary $\delta\bar{D}_{in}$ is shown in figure 14a and 14c. Note that the shape of these boundaries is particularly simple in this data set, because throughout the time span, the left and right boundaries have only inflow and outflow components, respectively. In figure 14c we build a parameterization $\bar{P}_t$ based on the time slice $t = 240$ and completing it with the appropriate parts of $\delta\bar{D}_{in}$ and $\delta\bar{D}_{out}$ to get a complete path line parameterization, as described in section 5.1. All three parameterizations are crossed by all path lines in the domain. Five of them are shown in figure 14. Note that they cross separating structures in all parameterizations. Therefore, they are material structures.

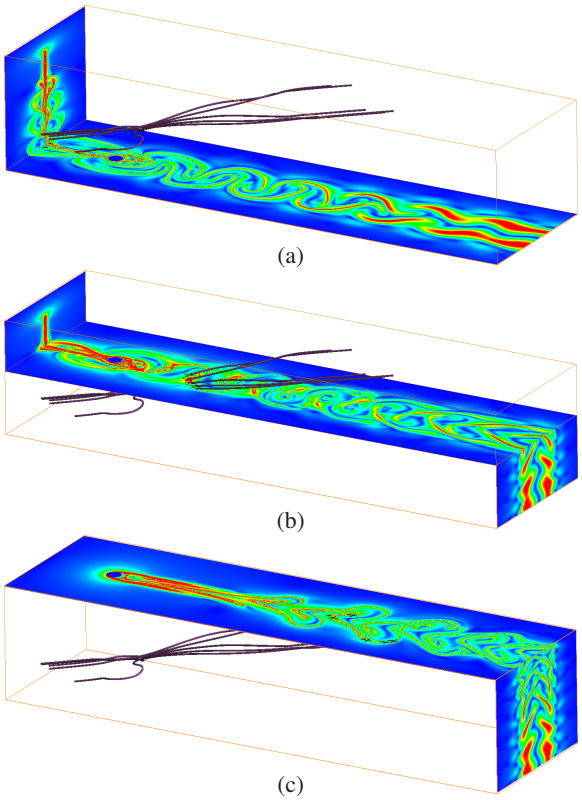

Figure 14: *MSF on parameterization subdomains of cylinder flow: (a) $\delta\bar{D}_{in}$, (b) $\bar{P}_t$ based time slice $t = 240$, (c) $\delta\bar{D}_{out}$. The dark lines are 5 different path lines.*

7. Discussion

We have analyzed that, in general, FTLE ridges are not material structures. At first sight, this is a contradiction to the results of Shadden et al. [SLM05], who found FTLE ridges to approximate material structures well. Shadden et al. also have shown that for $T \to \infty$ FTLE ridges become exact material lines, which on the other hand becomes equivalent to the infinite-time LE. In fact, our results for the double gyre with rather long integration time confirm the results of Shadden et al. However, for shorter integration times, the approximation error of FTLE becomes larger. In practice, we have to face the fact that we have data sets of limited time spans. Because FTLE is computed using constant integration times, FTLE methods rely on relatively short integration times in practical applications. With the cylinder data set we have shown that in such cases the approximation error can become substantial and the flux across FTLE ridges cannot be ignored. In contrast, we have shown that particles advected in the flow stay on separating structures of the MSF and these have zero cross flux. In conclusion, we agree with the result of Shadden et al. However, we found that the error for shorter integration times can become more substantial in practice.

Our method represents a modification of the FTLE method. While FTLE analyzes flow separation over a given time span, the MSF method incorporates the whole temporal extent of the data set and extracts true material structures as separating structures. Since at any time step t, the MSF is computed both from forward and backward integration of path lines, our results contain mixtures of unstable and stable manifolds. In section 5.3 we have presented an optional visualization technique to still differentiate between these structures. At the initial time steps, the separating structures from forward integration are dominant. Over the course of time, these structures compress and corresponding particles converge to the boundary. At the initial time steps, the particles on separating structures from backward integration are very

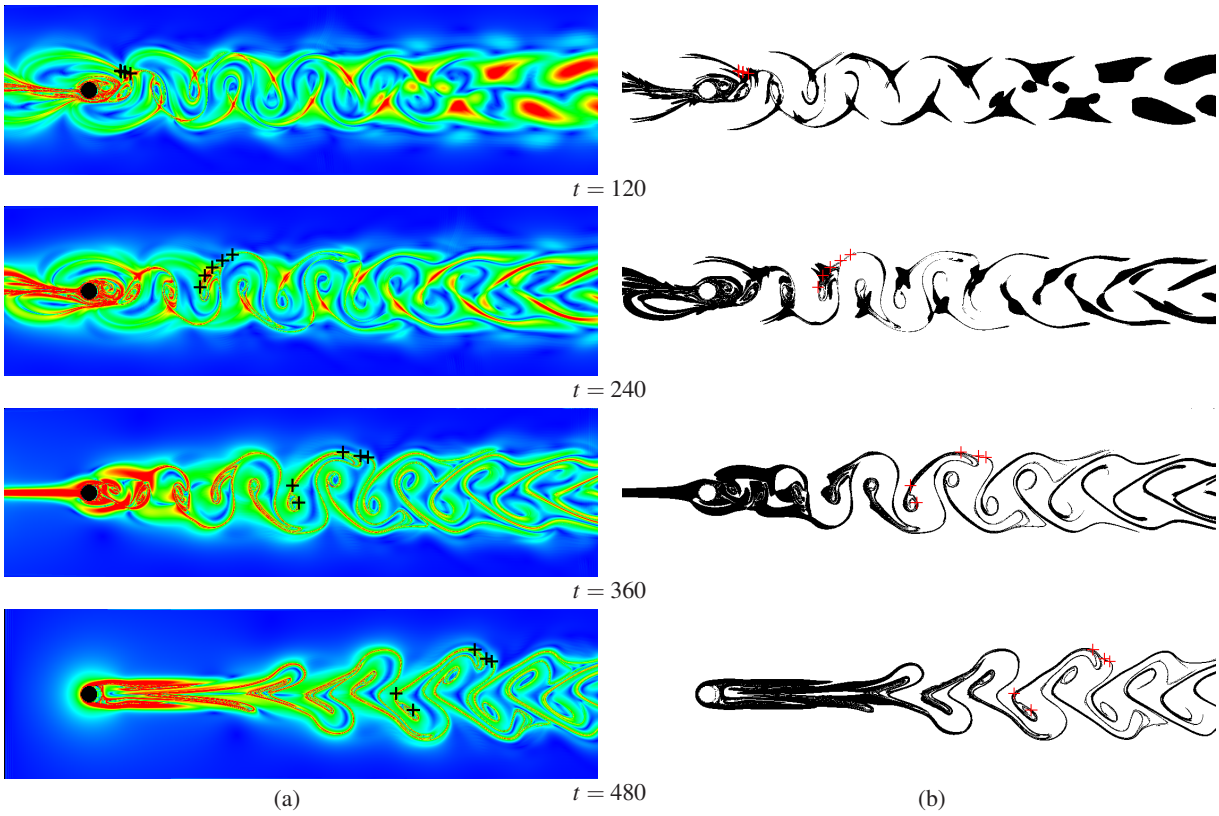

Figure 15: *Flow around a circular cylinder: (a) MSF, (b) MSF separating structures. The black and red crosses show particles advected by the flow.*

close to the boundary. In subsequent time steps they diverge from the boundary while the structures expand.

An advantage of our method is that the topology of the MSF is preserved over time. Hence, MSF separating structures consistently bound regions of coherent flow behavior throughout time. In contrast, FTLE values on a given path line are not constant. Thus, the topology of FTLE fields and ridges vary over time. Furthermore, for divergence-free vector fields the volume of MSF separating structures is invariant. The double gyre example (figure 11b) demonstrates this behavior.

With our method, the MSF value of any point $(\mathbf{x},t)$ in $\bar{D}$ can be found by computing the MSF values of a parameterization $\bar{P}$ as introduced in section 5.1 in preprocess and integrating a particle from $(\mathbf{x},t)$ to $\bar{P}$. This technique could be used for the rapid computation of MSF, which could serve for real-time exploration applications. However, the MSF values of $\bar{P}$ are computed at discrete samples. This can lead to artifacts caused by the insufficient resolution of computed MSF values. For instance, the folding of separating structures at the border of the double gyre example is hidden by a limited resolution of the sampled MSF.

8. Conclusion

We presented a novel technique called MSF based on a modification of the FTLE method. The main advantage of MSF separating structures over FTLE ridges is that they are material structures. Therefore, MSF values are constant along path lines. With MSF we can compute exact LCS of unsteady vector fields with finite time. We introduced a parameterization of path lines. Based on this parameterization and the invariance of MSF on path lines, we introduced a simple way to compute MSF values at every point in space-time. We proposed a definition for MSF separating structures that yields material structures. Hence, they consistently bound regions of coherent flow and have invariant topology.

For future work, we plan to build an interactive MSF exploration tool that computes the MSF in real time. In this context, we have to address the issue of the possibly insufficient sampling of $\bar{P}$. One way to solve this problem could be adaptive sampling of MSF. Another way would involve MSF on multiple parameterizations based on different time slices that reduce sampling artifacts. Our concept of MSF is not restricted to 2D data sets. In the future, we also want to cover the 3D case and apply our method to 3D data sets.

Acknowledgments

We thank Gabor Janiga from Otto-von-Guericke University for providing the cylinder data set. The work was partially funded by the Sem-Seg project under the EU FET-Open grant 226042 and by the German Ministry of Education and Science (BMBF) within the ViERforES project (no. 01IM08003C).

References

[CMLZ08] CHEN G., MISCHAIKOW K., LARAMEE R. S., ZHANG E.: Efficient morse decompositions of vector fields. *IEEE Transactions on Visualization and Computer Graphics 14* (July 2008), 848–862.

[EGM*94] EBERLY D., GARDNER R., MORSE B., PIZER S., SCHARLACH C.: Ridges for image analysis. *Journal of Mathematical Imaging and Vision 4*, 4 (1994), 353–373.

[GGTH07] GARTH C., GERHARDT F., TRICOCHE X., HAGEN H.: Efficient computation and visualization of coherent structures in fluid flow applications. *IEEE Transactions on Visualization and Computer Graphics 13*, 6 (2007), 1464–1471.

[GLT*09] GARTH C., LI G., TRICOCHE X., HANSEN C., HAGEN H.: Visualization of coherent structures in transient 2d flows. In *Topology-Based Methods in Visualization II*, Mathematics and Visualization. Springer Berlin Heidelberg, 2009, pp. 1–13.

[Hal01] HALLER G.: Distinguished material surfaces and coherent structures in three-dimensional fluid flows. *Physica D 149* (2001), 248–277.

[Hal02] HALLER G.: Lagrangian coherent structures from approximate velocity data. *Physics of Fluids 14*, 6 (2002), 1851–1861.

[HY00] HALLER G., YUAN G.: Lagrangian coherent structures and mixing in two-dimensional turbulence. *Physica D 147*, 3-4 (2000), 352–370.

[KPH*09] KASTEN J., PETZ C., HOTZ I., NOACK B., HEGE H.-C.: Localized finite-time lyapunov exponent for unsteady flow analysis. In *Vision Modeling and Visualization* (2009), Magnor M., Rosenhahn B., Theisel H., (Eds.), vol. 1, Universität Magdeburg, Inst. f. Simulation u. Graph., pp. 265–274.

[LCM*05] LEKIEN F., COULLIETTE C., MARIANO A. J., RYAN E. H., SHAY L. K., HALLER G., MARSDEN J.: Pollution release tied to invariant manifolds: A case study for the coast of florida. *Physica D 210*, 1 (2005), 1–20.

[LHZP07] LARAMEE R., HAUSER H., ZHAO L., POST F.: Topology-based flow visualization, the state of the art. In *Topology-based Methods in Visualization*, Mathematics and Visualization. Springer Berlin Heidelberg, 2007, pp. 1–19.

[Lia66] LIAPUNOV A. M.: *Stability of motion*. Academic Press, 1966.

[Lin98] LINDEBERG T.: Edge detection and ridge detection with automatic scale selection. *International Journal Computer Vision 30*, 2 (1998), 117–156.

[LM10] LIPINSKI D., MOHSENI K.: A ridge tracking algorithm and error estimate for efficient computation of lagrangian coherent structures. *Chaos: An Interdisciplinary Journal of Nonlinear Science 20*, 1 (2010), 017504.

[OBS04] OHTAKE Y., BELYAEV A., SEIDEL H.-P.: Ridge-valley lines on meshes via implicit surface fitting. *ACM Transactions on Graphics 23*, 3 (2004), 609–612.

[PS08] PEIKERT R., SADLO F.: Height Ridge Computation and Filtering for Visualization. In *Proceedings Pacific Vis* (2008), pp. 119 – 126.

[PVH*03] POST F. H., VROLIJK B., HAUSER H., LARAMEE R. S., DOLEISCH H.: The State of the Art in Flow Visualisation: Feature Extraction and Tracking. *Computer Graphics Forum 22*, 4 (2003), 775–792.

[SGSM08] SALZBRUNN T., GARTH C., SCHEUERMANN G., MEYER J.: Pathline predicates and unsteady flow structures. *The Visual Computer 24* (2008), 1039–1051.

[SLM05] SHADDEN S. C., LEKIEN F., MARSDEN J. E.: Definition and properties of lagrangian coherent structures from finite-time lyapunov exponents in two-dimensional aperiodic flows. *Physica D 212*, 7 (2005), 271–304.

[SLP*09] SHADDEN S. C., LEKIEN F., PADUAN J. D., CHAVEZ F. P., MARSDEN J. E.: The correlation between surface drifters and coherent structures based on high-frequency radar data in monterey bay. *Deep Sea Research Part II: Topical Studies in Oceanography 56*, 3-5 (2009), 161 – 172.

[SP07] SADLO F., PEIKERT R.: Efficient visualization of lagrangian coherent structures by filtered amr ridge extraction. *IEEE Transactions on Visualization and Computer Graphics (Proceedings Visualization) 13*, 6 (2007), 19–26.

[SP09] SADLO F., PEIKERT R.: Visualizing lagrangian coherent structures and comparison to vector field topology. In *Topology-Based Methods in Visualization II*, Mathematics and Visualization. Springer Berlin Heidelberg, 2009, pp. 15–29.

[SRP11] SADLO F., RIGAZZI A., PEIKERT R.: Time-dependent visualization of lagrangian coherent structures by grid advection. In *Topological Methods in Data Analysis and Visualization*, Mathematics and Visualization. Springer Berlin Heidelberg, 2011, pp. 151–165.

[STS10] SCHULTZ T., THEISEL H., SEIDEL H.-P.: Crease surfaces: From theory to extraction and application to diffusion tensor MRI. *IEEE Transactions on Visualization and Computer Graphics 16*, 1 (2010), 109–119.

[SW10] SADLO F., WEISKOPF D.: Time-Dependent 2D Vector Field Topology: An Approach Inspired by Lagrangian Coherent Structures. *Computer Graphics Forum 29*, 1 (2010), 88–100.

[SWTH07] SAHNER J., WEINKAUF T., TEUBER N., HEGE H.-C.: Vortex and strain skeletons in eulerian and lagrangian frames. *IEEE Transactions on Visualization and Computer Graphics 13*, 5 (2007), 980–990.

[TWHS05] THEISEL H., WEINKAUF T., HEGE H.-C., SEIDEL H.-P.: Topological methods for 2D time-dependent vector fields based on stream lines and path lines. *IEEE Transactions on Visualization and Computer Graphics 11*, 4 (2005), 383–394.

[WPJ*08] WELDON M., PEACOCK T., JACOBS G. B., HELU M., HALLER G.: Experimental and numerical investigation of the kinematic theory of unsteady separation. *Journal of Fluid Mechanics 611* (2008), 1–11.